8932 *Biochemistry* **2009,** *48,* 8932–8939
DOI: 10.1021/bi901150a

BIOCHEMISTRY
including biophysical chemistry & molecular biology
Accelerated Publication

Crystallographic and Catalytic Studies of the Peroxide-Shunt Reaction in a Diiron Hydroxylase[†]

Lucas J. Bailey and Brian G. Fox*

Department of Biochemistry, College of Agricultural and Life Sciences, University of Wisconsin, Madison, Wisconsin 53706-1544

Received July 7, 2009; Revised Manuscript Received August 10, 2009

ABSTRACT: A diiron hydroxylase reaction typically begins by combination of O_2 with a diferrous center to form reactive intermediates capable of hydrocarbon hydroxylation. In this natural cycle, reducing equivalents are provided by specific interactions with electron transfer proteins. The biological process can be bypassed by combining H_2O_2 with a diferric center, i.e., peroxide-shunt catalysis. Here we show that toluene 4-monooxygenase has a peroxide-shunt reaction that is ~600-fold slower than catalysis driven by biological electron transfer. However, the toluene 4-monooxygenase hydroxylase−effector protein complex was stable in the presence of 300 mM H_2O_2, suggesting overall benign effects of the exogenous oxidant on active site structure and function. The X-ray structure of the toluene 4-monooxygenase hydroxylase−effector protein complex determined from crystals soaked in H_2O_2 revealed a bound diatomic molecule, assigned to a *cis*-μ-1,2-peroxo bridge. This peroxo species resides in an active site position adjacent to the hydrogen-bonding substructure established by effector protein binding and faces into the distal cavity where substrate must bind during regiospecific aromatic ring hydroxylation catalysis. These results provide a new structural benchmark for how activated intermediates may be formed and dispatched during diiron hydroxylase catalysis.

Diiron hydroxylases are multicomponent enzyme complexes that require NADH and O_2 for in vivo catalysis (*1*−*3*). In addition to the hydroxylase, the T4MO[1] complex consists of an NADH oxidoreductase [T4moF (*4*)] that is responsible for transferring reducing equivalents from NADH to T4moC, a Rieske ferredoxin that directly and specifically reduces T4moH (*5*, *6*), and a cofactorless effector protein, T4moD (*7*, *8*). T4moD forms a high-affinity complex with T4moH to increase the rate of steady-state catalysis up to ~150-fold (*8*). Crystal structures of the T4moHD complex in the resting (diferric) and reduced (diferrous) states revealed a number of coordinated changes within the active site that occur upon complex formation (*9*) and presumably set the stage for efficient catalysis.

sMMO, another diiron hydroxylase, has a well-characterized catalytic cycle (Figure 1), and many supporting spectroscopic and structural studies of it have been completed (*1*−*3*). Reaction of diferrous sMMO (Figure 1B) with O_2 produces a peroxo-diferric species named compound P (Figure 1C), which is the first spectroscopically detected intermediate along the hydroxylation reaction cycle (*10*). Compound P has been proposed to be competent for alkene epoxidation (*11*). Compound P also reacts to form a high-valent diferryl intermediate named compound Q (Figure 1D), which is chemically competent for methane and norcarane hydroxylation (*12*, *13*). Upon product release, the active site assumes the resting-state diferric configuration until effector protein binding and reduction begin another catalytic cycle (*12*).

In diferric sMMO, O_2-mediated turnover was successfully bypassed by reaction with H_2O_2 (*14*). This reaction, called the peroxide shunt, presumably proceeded via direct formation of a compound P-like species (*15*). sMMO was capable of at least 30 turnovers with propene during peroxide-shunt catalysis with a rate of ~1 s^{-1}, which is comparable to the rate observed with O_2-mediated turnover.

Recently, a different type of peroxo-diferric intermediate has been proposed for the toluene/*o*-xylene monooxygenase reaction (*16*). The Mössbauer isomer shift of this species was consistent with a diferric assignment, but the absence of a visible absorption feature indicated that the ToMOH species was somehow distinct from the peroxo-diferric species observed in sMmoH (*10*), ribonucleotide diphosphate reductase R2 component (*17*), stearoyl-ACP Δ^9-desaturase (*18*), ferritin (*19*), deoxyhypusine hydroxylase (*20*), or hemerythrin (*21*).

Although a number of informative catalytic studies have been performed with members of the toluene monooxygenase family (*5*, *8*, *22*−*24*), the experimental establishment of a peroxide-shunt reaction has been unsatisfactory. Thus, variable levels of catalase activity have been observed in both native (*25*) and recombinant enzyme preparations (*5*, *16*), and this has

[†]This work was funded by National Science Foundation Grants MCB-0316232 and MCB-0843239 to B.G.F. Use of the Advanced Photon Source was supported by the U.S. Department of Energy, Basic Energy Sciences, Office of Science, under Contract W-31-109-ENG-38. Use of the Life Science Collaborative Access Team at the Advanced Photon Source was supported by the College of Agricultural and Life Sciences, Department of Biochemistry, and Graduate School of the University of Wisconsin.

*To whom correspondence should be addressed: Department of Biochemistry, 433 Babcock Dr., University of Wisconsin, Madison, WI 53706. Phone: (608) 262-9708. Fax: (608) 262-3453. E-mail: bgfox@biochem.wisc.edu.

[1]Abbreviations: T4MO, four-protein toluene 4-monooxygenase complex from *Pseudomonas mendocina* KR1; T4moH, hydroxylase component of T4MO; T4moD, effector protein of T4MO; T4moHD, stoichiometric complex of T4moH and T4moD; T4moC, Rieske-type ferredoxin of the T4MO complex; T4moF, NADH oxidoreductase of the T4MO complex; sMMO, soluble methane monooxygenase; sMmoH, sMMO hydroxylase component; ToMO, toluene/*o*-xylene monooxygenase; ToMOH, ToMO hydroxylase; PDB, Protein Data Bank.

 Published on Web 08/25/2009 © 2009 American Chemical Society

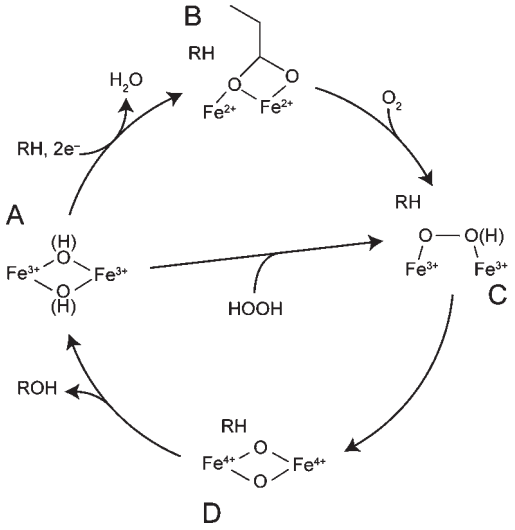

FIGURE 1: Representative reaction cycle for the diiron hydroxylases. In T4moHD, substrate binding is thought to occur prior to the formation of activated intermediates. The resting diferric state (A) is reduced by $2e^-$ concomitant with rearrangement of a carboxylate ligand and displacement of a bridging water molecule. The diferrous center (B) reacts with O_2 to generate the peroxo-diferric state (C). Alternatively, the peroxide-shunt pathway proceeds by combination of the diferric state (A) and H_2O_2 to also form a peroxo-diferric state (C). Because of differences in the proton balance within the active site, the peroxo-diferric states initially formed by these two different pathways may not be equivalent. Reaction of the peroxo-diferric state yields a diferryl intermediate (D). The diferryl intermediate reacts with substrate, RH, to generate a hydroxylated product, ROH.

complicated the characterization of peroxide-shunt reactions. In this work, enzyme prepared for X-ray crystallographic studies was used to characterize the peroxide-shunt reaction of T4moH alone, and the complex of T4moH and T4moD (T4moHD) without the biological electron transfer partners T4moF, T4moC, and NADH. These newest preparations have ~100-fold lower catalase activity than previously observed (*5*). In these preparations, the H_2O_2-dependent formation of *p*-cresol was slow but continued in the presence of 300 mM H_2O_2 without loss of activity for an extended time period, suggesting a structurally robust active site. With this solution-state catalytic information, crystals of the T4moHD complex were prepared, treated with H_2O_2, and frozen for X-ray diffraction studies. The presented crystal structure reveals an active site geometry corresponding to a frequently hypothesized H_2O_2-level precursor to diiron enzyme reaction intermediates. Some of the implications of this observation are discussed.

MATERIALS AND METHODS

Expression, Purification, and Crystallization. All T4MO components were expressed and purified as previously described (*4*, *6*, *7*, *26*). T4moH used in crystallization trials was pooled on the basis of activity and strictest criteria for purity as determined by SDS−PAGE to minimize contaminating proteins. This resulted in an ~50% decrease in the yield of purified protein as compared to previous studies. Crystals of T4moHD in the absence of acetate were obtained from hanging drop vapor diffusion by adding 2.5 μL of 140 μM T4moH and 280 μM T4moD to 2.5 μL of 100 mM Bis-Tris (pH 6.0) containing 24% PEG 3350 and 200 mM NH_4Cl. Crystals were generally obtained by seeding with a stock of crystals produced under the previously reported conditions (*9*). Prior to cryoprotection, crystals were soaked in a solution of mother liquor supplemented with 300 mM H_2O_2 for ~20 min. Crystals were cryoprotected by incrementally increasing the precipitant to 30% PEG 3350, 700 mM NH_4Cl, and 300 mM H_2O_2 and were frozen by rapid immersion in liquid N_2 and then stored in liquid N_2.

Table 1: Kinetic Characterization of the T4moH Peroxide-Shunt Reaction

reaction	k_{cat} (min^{-1})	$K_m(H_2O_2)$ (mM)	ref
T4moHD O_2 turnover[a]	168	na[c]	*8*
T4moH O_2 turnover[a]	7.8	na[c]	*8*
T4moHD peroxide shunt[b]	0.30 (0.05)	128 (7)	this work
T4moH peroxide shunt[b]	0.27 (0.05)	122 (10)	this work

[a]O_2-mediated turnover reactions conducted with optimized concentrations of T4moH, T4moD, T4moC, and T4moF in the presence of saturating toluene, NADH, and O_2. [b]Peroxide-shunt reactions conducted with T4moH or T4moHD in the presence of saturating toluene and varying levels of H_2O_2. [c]Not applicable.

Kinetic Assays. Reactions were performed at 26 °C with 10 μM T4moH and variable amounts of T4moD and T4moC. Reactions were initiated by the addition of H_2O_2 to a crimp-sealed vial and allowed to continue for up to 3 h. Reaction contents were quenched in NaCl-saturated HCl and prepared and quantified as previously described (*8*). Optical spectra of T4moHD reactions were recorded during this time duration using an Agilent diode array spectrophotometer (Agilent Technologies, Santa Clara, CA) or an Olis RSM stopped-flow device (OLIS, Inc., Bogart, GA).

Structure Determination. Diffraction data were collected on Advanced Photon Source (Argonne, IL) Life Science Collaborative Access Team beamline 21-ID-F. The data were indexed, integrated, and scaled using HKL2000 (*27*). The structure was determined by molecular replacement with the CCP4 suite program MOLREP (*28*) using PDB entry 3HDH as the starting model. Simulated annealing was performed in PHENIX (*29*) followed by iterative rounds of model fitting and refinement in COOT (*30*) and REFMAC5 (*31*), respectively. Ramachandran analysis and rotamer analysis were performed with Molprobity (*32*). Figures were prepared with PyMOL (*33*).

RESULTS

Peroxide-Shunt Catalysis. During O_2-dependent catalysis, the effector protein T4moD was responsible for up to ~30-fold enhancement of the rate of T4MO steady-state turnover and also contributed to control of regiospecificity of aromatic ring hydroxylation (*8*). In contrast, Table 1 shows that the rate of peroxide-shunt catalysis did not substantially change either with or without T4moD.

The initial rate of product formation was ~0.3 min^{-1}, which is ~600-fold lower than the rate of product formation obtained with the optimized biological electron transfer chain. During peroxide-shunt catalysis in the presence of 300 mM H_2O_2, hydroxylated cresol products continued to accumulate for >1 h, which is comparable to the duration observed for peroxide-shunt activity of sMmoH (*14*). The product distribution observed throughout the time course was typical of the T4moH-catalyzed reaction in the absence of T4moD, i.e., 55% *p*-cresol, 43% *o*-cresol, 2% *m*-cresol, and a barely detectable content of benzyl alcohol (Table 2). These results are contrasted with those of nonenzymic electrophilic aromatic substitution reactions, which favor ortho or benzylic hydroxylation (*34*). The role of

Table 2: Product Distributions from Peroxide-Shunt and Biological Turnover Reactions

reaction	*o*-cresol	*p*-cresol	*m*-cresol	benzyl alcohol	ref
T4moHD peroxide shunt[a]	43	55	2	nd[c]	this work
T4moHD biological O_2 turnover[b]	2	96	1	1	*8*
T4moH peroxide shunt[a]	43	55	2	nd[c]	this work
T4moH biological O_2 turnover[b]	63	6	16	15	*8*
G103L T4moHD peroxide shunt[a]	38	45	16	nd[c]	this work
G103L T4moHD biological O_2 turnover[b]	55	24	20	1	*8*

[a]Peroxide-shunt reactions conducted with T4moH or T4moHD in the presence of saturating toluene and 300 mM H_2O_2. [b]O_2-mediated turnover reactions conducted with optimized concentrations of T4moH, T4moD, T4moC, and T4moF in the presence of saturating toluene, NADH, and O_2. [c]Not detected, which may reflect the combination of a low percentage of formation and slow turnover in the peroxide-shunt reaction.

Table 3: Summary of Data Collection, Crystal Structure, and Refinement Statistics

	resting T4moHD, no acetate (3I5J)	peroxide-bound T4moHD (3I63)
space group	$C222_1$	$C222_1$
wavelength (Å)	0.97872	0.97872
crystal dimensions (Å)	100.4 × 115.7 × 181.3	98.8 × 116.9 × 181.6
resolution range (Å)[a]	90.54−1.90 (1.95−1.90)	90.91−2.09 (2.14−2.09)
no. of unique (total) reflections	76944	58828
R_{merge}	0.068 (0.436)	0.071 (0.124)
completeness (%)	97.44 (86.52)	99.25 (92.60)
no. of non-hydrogen atoms[b]	8809	17481
no. of solvent molecules	753[e]	639[f]
R (working)[c]	0.157 (0.297)	0.160 (0.154)
free *R* value[d]	0.207 (0.299)	0.209 (0.212)
mean *B* value (Å^2)	14.6	21.2
Ramachandran plot (%)		
favored	97.8	97.6
additionally allowed	2.2	2.4
disallowed	0	0
root-mean-square deviation		
bond lengths (Å)	0.023	0.022
bond angles (deg)	1.814	1.758

[a]Numbers in parentheses indicate the highest-resolution shell of 20. [b]Number of non-hydrogen atoms included in refinement. [c]$R = \sum||F_o| - |F_c||/\sum|F_o|$, where $|F_o|$ is the observed structure factor amplitude and $|F_c|$ is the calculated structure factor amplitude. [d]$R_{free} = R$ calculated on the basis of exclusion of 5.1% of the data from the refinement. [e]Includes 753 water molecules. [f]Includes 639 water molecules.

the active site in the peroxide-shunt-mediated hydroxylation was further supported by the altered regiospecificity of the G103L T4moHD complex, which afforded 16% *m*-cresol in the peroxide shunt, a level significantly higher than that found in the wild-type isoform or in solution reactions. This increased yield of *m*-cresol is comparable to the 20% *m*-cresol observed from G103L T4moHD during O_2-mediated turnover (Table 2).

No absorbance in the visible region was observed from either steady-state or rapid-mix reactions of T4moHD with H_2O_2. Moreover, the rate of the peroxide-shunt reaction did not exhibit a logarithmic dependence on the pH of the reaction, suggesting that changes in the protonation state of reactive intermediates did not represent a rate-limiting step over the pH range of 6−8.5.

Crystallization Conditions. Crystallization conditions used in many past studies of diiron hydroxylases have included acetate or other small molecule carboxylates (*9*, *35*−*37*). These additives are often found in the active site and are often coordinated to the diiron center as bridging ligands. In anticipation that these bound additives might act as inhibitors of catalysis, we undertook a systematic search for crystallization conditions that did not include small molecule carboxylate ligands and identified the conditions used in this work. Using crystals prepared in this new precipitant solution, the structure of T4moHD was determined at 1.9 Å resolution without acetate in the crystallization buffer.[2] Table 3 provides a summary of the structure determination statistics for this new structure, and Figure 2 provides a side-by-side comparison of the active sites. In summary, except for replacement of a coordinated acetate molecule with a loosely coordinated water molecule, the structures of resting T4moHD crystallized in either the presence (Figure 2A) or the absence (Figure 2B) of acetate are equivalent, including the positions of all active site ligands.

Structure of Peroxo-T4moHD. Incubation of resting T4moHD crystals with 300 mM H_2O_2 for ∼30 min yielded no appearance of color and afforded diffraction at ∼2.1 Å. Table 3 provides a summary of structure determination statistics for this complex, while Figure 2 shows a side-by-side comparison of the active sites in resting acetate-free T4moHD (Figure 2B) and in peroxo-T4moHD (Figure 2C). Overall, the acetate-free and peroxo-T4moHD structures had a 0.2 Å root-mean-square deviation (rmsd) for alignment of the 490 residues in the comparable TmoA subunits that contain the active site. With the exception of the exchangeable coordination site occupied by acetate, water, or H_2O_2, the diiron center ligands in these two structures were superimposable.

[2]Coordinates and structure factors of structures reported herein have been deposited in the PDB as entries 3I5J (resting T4moHD crystallized in the absence of acetate) and 3I63 (resting T4moHD treated with H_2O_2).

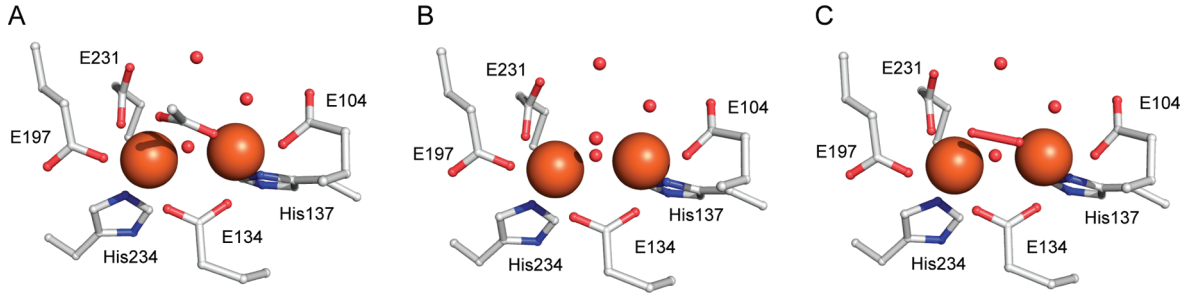

FIGURE 2: T4moHD complex active sites. (A) Crystals prepared with acetate in crystallization buffer. (B) Crystals prepared without acetate in crystallization buffer. (C) Peroxo-T4moHD. The active site water molecules are represented as red spheres, and the peroxide moiety of panel C is shown in a red stick representation.

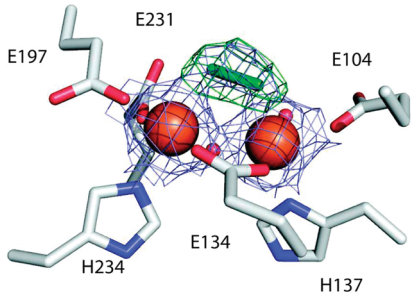

FIGURE 3: Model for the active site of peroxo-T4moHD. An omit map of the peroxide species is shown with the $2F_o-F_c$ map (slate) contoured to 2σ and the F_o-F_c map (green) contoured to 5σ.

With the peroxo-T4moHD crystals, a $2F_o - F_c$ difference map revealed an elongated feature of electron density that bridged between the iron atoms of the diiron center. This feature was located on the face of the diiron center opposite to the histidine ligands and projected toward the inner cavity of the active site, where the substrate must bind during catalysis.

This electron density was modeled using several different assumptions for its identity. When modeled as a single water molecule, substantial residual density was unaccounted for along the Fe−Fe vector, suggesting that this feature might correspond to a diatomic species. Modeling with two waters was likewise not satisfactory, as the interatomic distance of 1.8 Å was also incompatible with the volume typically required to hold these two molecules.

When the difference density was modeled as H_2O_2 using an O−O bond distance restraint of 1.5 Å and 70% occupancy, the resulting best fit gave Fe−O distances of ~2.2 and 2.4 Å and *B* factors (~19 Å^2) within the range of the other protein-derived atoms assembling the primary coordination sphere of the active site (~10−28 Å^2). As an alternative, when the O−O distance restraint was released, the resulting best model of the difference density increased the O−O distance to 1.8 Å, yielded compensating decreases in the Fe−O distances to ~2.1 Å, and yielded slight decreases in the temperature factors. In both models, the peroxide moiety was bound in a μ-1,2 bridging mode with a dihedral angle of ~29°.

Figure 3 shows a close-up representative electron density and the modeled structure of peroxo-T4moHD obtained using the O−O bond distance restraint of 1.5 Å. The Fe−Fe distance of 3.4 Å was not significantly altered relative to the resting structure. HOH2, normally displaced by the shift of Glu231 into the bridging position upon reduction of the diferric center (*9*), was still present. Likewise, HOH3 was bound to Fe1, and HOH5 was positioned by interactions with Thr201, Glu231, Gln228, and HOH3 (see Hydrogen-Bonding Substructure and Figure 4). The positions of all other coordinating protein ligands were identical.

Hydrogen-Bonding Substructure. The crystal structure of resting T4moHD (*9*) revealed that a unique water molecule, HOH5, was localized by a T4moD-induced rearrangement of the active site. The hydrogen-bonding substructure produced by this rearrangement notably includes Thr201, Gln228, Glu231, and HOH2, the latter of which is coordinated to Fe1 and also hydrogen-bonded by Glu104. Figure 4 shows that the peroxo species is intimately associated with this substructure. Thus, the peroxo O atom bound to Fe1 moved within 3.1 Å of HOH3 and within 3.6 Å of the unbound carboxylate O of Glu231, which was also within 2.7 Å of HOH5.

Along with the previously noted residues Thr201, Asn202, and Glu231, residues Gln141, Phe205, and Ile227 provide the boundary surface for the internal cavity holding HOH3 and HOH5 in place. The aromatic ring of Phe205 provides the majority of this surface, including the provision of van der Waals contacts with HOH5, while the amide O atom of Gln141 is oriented toward the unbound carboxyl O atom of Glu104, thus extending the interactions with HOH3.

DISCUSSION

This work has provided new insight into the types of intermediates that may form in diiron enzymes and features of the enzyme active site that may control their reactivity.

Enzymic Peroxide-Shunt Reaction. The rates of product formation in the T4moH and T4moHD peroxide-shunt reactions were ~600-fold slower than the rate of the reaction caused by O_2-mediated turnover, and this work suggests reasons why this might be so. Monooxygenase reactions ultimately require the delivery of two protons during the reduction of one O atom to water (*38*). Figure 4 shows a hydrogen-bonded substructure of T4moHD that is apparently optimized for reaction of the diferrous center with O_2, which must include efficient delivery of protons. Our cumulative structural evidence indicates that this hydrogen-bonded substructure forms upon T4moHD binding (*9*) and persists after two-electron reduction of the diiron center. By reliance on H_2O_2 as both the electron donor and the source of O atoms for the hydroxylation reaction, the peroxide-shunt reaction increases the inventory of protons in the active site beyond that required for the optimal reaction. Specifically, two protons must be released from H_2O_2 to facilitate binding to the diferric center. Accommodation of this different proton count represents one way that the peroxide-shunt reaction will differ from the biological reaction and perhaps lead to altered rates of reaction.

This work shows that bridging HOH2 was retained in peroxo-T4moHD, apparently because the reduction-driven rearrangement

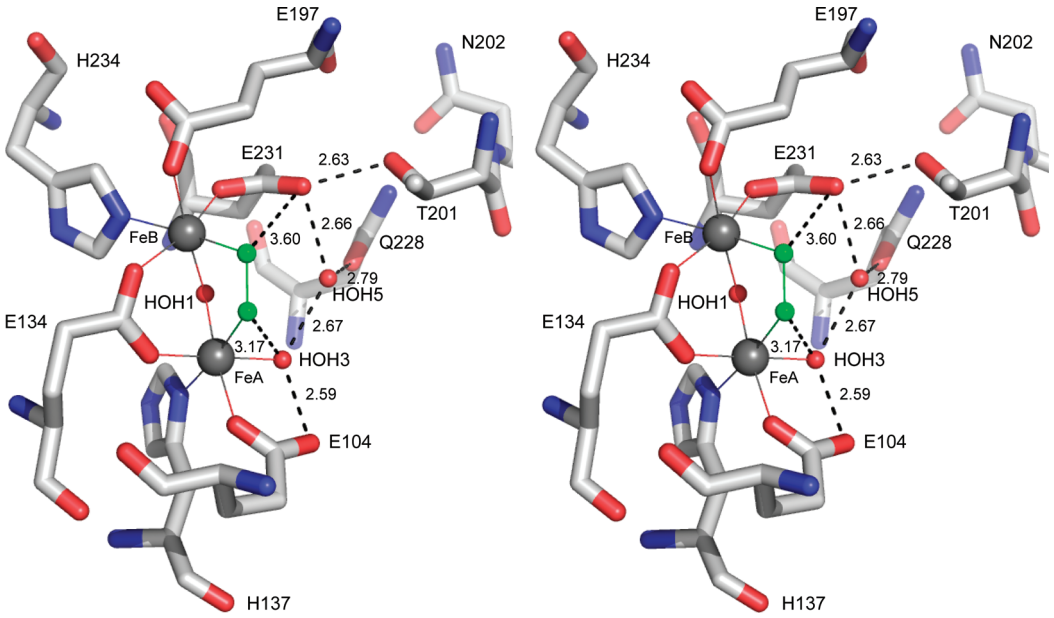

FIGURE 4: Stereoview of the active site of peroxo-T4moHD showing the hydrogen-bonding substructure possibly involved in the delivery of two protons that fulfill the stoichiometry of the monooxygenase reaction. The peroxo molecule is colored green; active site residues and selected bond distances are shown.

Table 4: Properties of Non-Heme Iron−Peroxo Complexes in Enzymes and Model Complexes

complex	PDB entry	O−O distance (Å)	M1—O distance (Å)	M2—O distance (Å)	dihedral angle (deg)	comments	ref
peroxo-T4moHD	3I63	1.5	2.2	2.4	29		this work
oxy-hemerythrin	1hmo	1.5	2.1	na[a]	na[a]	peroxo species	*45*
naphthalene dioxygenase	1o7m	1.4	2.2; 2.3	na[a]	na[a]	O_2-bound complex	*46*
	1o7n	1.5	1.7; 2.0	na[a]	na[a]	O_2, substrate complex	
2,3-homoprotocatechuate dioxygenase	2iga:c	1.3	2.4; 2.5	na[a]		superoxo species	*47*
	2iga:b,d	1.5	2.1	na[a]	na[a]	alkylperoxo species	
cysteine dioxygenase	3eln	1.5	2.1	na[a]	na[a]	putative persulfenate complex	*48*
$[Fe_2(\mu\text{-}1,2\text{-}O_2)(N\text{-}Et\text{-}hptb)(Ph_3PO)^2]^{3+}$		1.42	1.88	1.88	~0		*49*
$[Fe_2(Ph\text{-}bimp)(C_6H_5COO)(O_2)]^{2+}$		1.43	1.94	1.86	9.9	first diiron-O_2 adduct complex crystallographically characterized	*50*
$[Fe_2(\mu\text{-}O_2)(\mu\text{-}O_2CCH_2Ph)_2(HB(pz'_3)_2]$		1.41	1.91	1.88	53.5	model complex with Mössbauer parameters comparable to those of H_{peroxo}	*42*

[a]Not applicable.

of Glu231 had not yet occurred. The presence of a bridging hydroxide has been previously proposed to stabilize metal-bound peroxo species (*20*). In possible correspondence with these results, the presence of HOH2 may contribute to the stability of peroxo-T4moHD. Furthermore, calculations by Friesner and co-workers suggest that both O atoms in oxy-diferryl intermediates such as compound Q derive from O_2 (*40*), further supporting the hypothesis that a water (or hydroxide) bridge such as HOH2 will not be present in the most reactive diiron intermediates.

The rearrangement of Glu231 in T4moHD is apparently responsible for the displacement of bridging water HOH2. Moreover, the acetate-free structure of T4moHD shows two open coordination sites on the iron atoms facing toward the presumed substrate-binding site. This would be an attractive position for O_2 to coordinate and react during catalysis. Occupation of the open coordination sites by peroxide prior to the carboxylate shift of Glu231 may alter the kinetics of this rearrangement, representing another deviation in the catalytic pathway relative to the biological reaction. In this regard, a recently determined structure of reduced T201A T4moHD revealed that Glu231 was primarily not in the bridging position (*41*), although residual electron density near HOH2 suggested the ability of Glu231 to transiently achieve this active site arrangement in the mutated enzyme. Since the rate of formation of the product of T201A T4moHD was ~3−6-fold faster for all substrates tested, we postulated that ligand rearrangements may contribute rate-limiting steps to the catalytic cycle.

One other facet of the peroxide-shunt reaction warrants a mention. Previous single-turnover studies of sMmoH revealed that product release was the slowest step during the turnover of nitrobenzene (*12*). As this step was slower than steady-state turnover, Lipscomb and co-workers proposed that reduction of the diiron center might play a role in product release. This might also be true for T4moH catalysis, reflecting the different affinities of Fe^{2+} and Fe^{3+} for the phenoxide (or phenol) bound in the active site as the ending step in the catalytic reaction.

Geometric Properties of Peroxo-T4moHD. Table 4 summarizes the properties of non-heme peroxo-iron species observed in T4moHD, other enzymes, and model complexes. By assuming a peroxo O−O bond distance of 1.5 Å, we found crystallographic

model refinement gave peroxo Fe−O bond distances of ~2.2 Å for peroxo-T4moHD. These are longer than the bonds observed in small molecule complexes, where the peroxo Fe−O bonds are generally ~1.85−1.95 Å in length. Moreover, Fe−O bond lengths of ~1.9 Å were predicted for sMmoH compound P by DFT calculations (*39*, *40*). We also investigated whether a longer O−O bond was compatible with the observed electron density, and crystallographic model refinement gave an unreasonably long O−O bond length of 1.8 Å for peroxide but also gave a compensatory shortening of Fe−O bonds to ~2.1 Å.

Differences in the metal, ligand, and proton inventories in these various structures may account for some of these differences in bond lengths. Specifically, protonation of an active site-bound peroxide species may result in a lengthening of the metal−peroxide bonds (*39*) and consequent weaker coordination of the hydroperoxide ligand to the metal center. The absence of a detectable optical spectrum from peroxo-T4moHD may be rationalized in this manner, since protonation and weak coordination may both diminish the intensity of charge transfer interactions. These considerations may also apply to the colorless peroxo-diferric intermediate recently described in ToMOH (*16*).

The dihedral angle observed in peroxo-T4moHD is 29°. For the sake of comparison, Solomon and co-workers (*39*) predicted dihedral angles for peroxo-R2 of 37°, close to that observed in peroxo-T4moHD. Furthermore, among the peroxo-diferric model complexes characterized by X-ray crystallography (Table 3), the dihedral angles ranged from near planarity to ~52°. Interestingly, the model complex with Mössbauer parameters most similar to those of sMmoH compound P (*42*) had a dihedral angle of ~52°, also near the range predicted by DFT calculations.

Additional electron density was observed in the active site channel of peroxo-T4moHD. When it was modeled as H_2O_2, the *B* factor of this additional peroxide was 42 Å^2 at full occupancy and the nearest O atom was located 3.0 Å from the metal-bound peroxide species. These parameters are consistent with the presence of multiple H_2O_2 molecules in the active site channel, corresponding to the 300 mM H_2O_2 solution used to treat the crystals.

Reactivity. The identification of bound H_2O_2 in a T4moHD crystal structure suggests a level of stability exceeding that expected for the intermediates used in solution catalysis. However, it is known that reactions in crystals are slower than reactions in solution (*43*). Moreover, the high concentration of H_2O_2 present in the crystallization buffer, the apparently unique slowness of the peroxide-shunt reaction in T4moHD, the absence of substrate, and the use of a low temperature have likely contributed to the trapping of this precursor state. Alternatively, photoreduction of a quasi-stable peroxo-diferric center in the X-ray beam may have generated a stable, closely associated peroxo-diferrous complex or a hydroperoxo- or superoxo-mixed valence complex within the constraints of the frozen enzyme active site. Regardless of the formal electronic assignment of the density identified, considerable new geometrical information has been revealed by these results.

Hydrogen-Bonding Substructure. The monooxygenase reaction requires delivery of two protons during the reductive conversion of one atom from O_2 into water. The prior crystal structure of resting T4moHD revealed that a unique water molecule, HOH5, was localized by the hydrogen-bonding substructure produced by effector protein-induced rearrangement of Thr201, Gln228, the conformationally flexible carboxylate of Glu231 bound to Fe2, and HOH2, which is coordinated to Fe1 and is further positioned by hydrogen bonding to Glu104. With the exception of the reduction-induced shift of the side chain of Glu231, this network is retained upon two-electron reduction of the T4moHD complex, suggesting it represents a catalytically relevant active site substructure capable of delivering the proper number of protons required for the monooxygenase reaction.

The positioning of these proton donors around the peroxo-diiron core is chemically asymmetric, consisting of entry points defined either by HOH3, Glu104, and Gln141 or by HOH5, Thr201, Gln228, and Glu231. Asymmetric proton donation has been suggested as a mechanism for the promotion of heterolytic cleavage of the O−O bond during sMmoH catalysis (*38*). The current structure provides a plausible basis for this asymmetry and thus suggests a heterolytic cleavage of the O−O bond during T4moH catalysis as well (*41*).

Currently undefined features in the active sites of sMmoH, ToMOH, and T4moHD must manifest themselves in the differences in their catalytic properties. Interestingly, a species with Mössbauer spectroscopic parameters similar to those of the peroxo-diferric intermediate found in ToMOH (*16*) was observed in ribonucleotide reductase R2 protein (*44*). Bollinger and co-workers proposed this colorless intermediate might be a μ-1,1-hydroperoxo-diferric species that formed rapidly, kinetically masking the accumulation of an unprotonated, colored *cis*-μ-1,2-peroxo species like sMmoH compound P. Assuming rearrangements of peroxo-diferric species are required for catalysis, displacement of a bridging HOH2 might become the rate-limiting step relative to rearrangement of Glu231 during peroxide-shunt catalysis. Correspondingly, the presence of a bridging oxo/hydroxo moiety was recently invoked to explain the stability of a peroxo-diferric intermediate in deoxyhypusine hydroxylase (*20*).

CONCLUSION

The ability to produce and manipulate crystals of T4moHD has opened new avenues to investigating the relationship between diiron hydroxylase structure and catalytic function. The catalytic results presented here show that T4moHD is capable of peroxide-shunt catalysis characteristic of other representatives in the diiron enzyme family, albeit slowly. T4moHD exhibited a surprising stability in the presence of the exogenous oxidant and gave a product regiospecificity for the peroxide shunt consistent with an enzyme-catalyzed reaction. Treatment of resting crystals of T4moHD with H_2O_2 revealed an enzyme-bound μ-1,2 bridging peroxo species with structural properties reminiscent of those envisioned from spectroscopic studies, calculations, and synthetic model chemistry. The peroxo moiety is located immediately adjacent to an asymmetric hydrogen-bonding substructure and projects into the active site cavity where substrates must bind. This work provides a new structural benchmark along the diiron enzyme reaction pathway, likely residing between the diferrous enzyme and subsequent intermediates capable of hydrocarbon hydroxylation.

SUPPORTING INFORMATION AVAILABLE

Difference electron density for peroxo-T4moHD (Figure S1) and electron density assigned to a second peroxide molecule in the peroxo-T4moHD active site (Figure S2). This material is available free of charge via the Internet at http://pubs.acs.org.

REFERENCES

1. Merkx, M., Kopp, D. A., Sazinsky, M. H., Blazyk, J. L., Muller, J., and Lippard, S. J. (2001) Dioxygen activation and methane hydroxylation by soluble methane monooxygenase: A tale of two irons and three proteins. *Angew. Chem., Int. Ed. 40*, 2782–2807.
2. Wallar, B. J., and Lipscomb, J. D. (1996) Dioxygen activation by enzymes containing binuclear non-heme iron clusters. *Chem. Rev. 96*, 2625–2658.
3. Solomon, E. I., Brunold, T. C., Davis, M. I., Kemsley, J. N., Lee, S. K., Lehnert, N., Neese, F., Skulan, A. J., Yang, Y. S., and Zhou, J. (2000) Geometric and electronic structure/function correlations in non-heme iron enzymes. *Chem. Rev. 100*, 235–350.
4. Bailey, L. J., Elsen, N. L., Pierce, B. S., and Fox, B. G. (2008) Soluble expression and purification of the oxidoreductase component of toluene 4-monooxygenase. *Protein Expression Purif. 57*, 9–16.
5. Pikus, J. D., Studts, J. M., Achim, C., Kauffmann, K. E., Munck, E., Steffan, R. J., McClay, K., and Fox, B. G. (1996) Recombinant toluene-4-monooxygenase: Catalytic and Mossbauer studies of the purified diiron and Rieske components of a four-protein complex. *Biochemistry 35*, 9106–9119.
6. Moe, L. A., Bingman, C. A., Wesenberg, G. E., Phillips, G. N. Jr., and Fox, B. G. (2006) Structure of T4moC, the Rieske-type ferredoxin component of toluene 4-monooxygenase. *Acta Crystallogr. D62*, 476–482.
7. Lountos, G. T., Mitchell, K. H., Studts, J. M., Fox, B. G., and Orville, A. M. (2005) Crystal structures and functional studies of T4moD, the toluene 4-monooxygenase catalytic effector protein. *Biochemistry 44*, 7131–7142.
8. Mitchell, K. H., Studts, J. M., and Fox, B. G. (2002) Combined participation of hydroxylase active site residues and effector protein binding in a para to ortho modulation of toluene 4-monooxygenase regiospecificity. *Biochemistry 41*, 3176–3188.
9. Bailey, L. J., McCoy, J. G., Phillips, G. N. Jr., and Fox, B. G. (2008) Structural consequences of effector protein complex formation in a diiron hydroxylase. *Proc. Natl. Acad. Sci. U.S.A. 105*, 19194–19198.
10. Liu, K. E., and Lippard, S. J. (1995) Characterization of a diiron(III) peroxide intermediate in the reaction cycle of methane monooxygenase hydroxylase from *Methylococcus capsulatus* (Bath). *J. Am. Chem. Soc. 117*, 4997–4998.
11. Beauvais, L. G., and Lippard, S. J. (2005) Reactions of the peroxo intermediate of soluble methane monooxygenase hydroxylase with ethers. *J. Am. Chem. Soc. 127*, 7370–7378.
12. Lee, S. K., Fox, B. G., Froland, W. A., Lipscomb, J. D., and Munck, E. (1993) A transient intermediate of the methane monooxygenase catalytic cycle containing an Fe(IV)Fe(IV) cluster. *J. Am. Chem. Soc. 115*, 6450–6451.
13. Brazeau, B. J., Austin, R. N., Tarr, C., Groves, J. T., and Lipscomb, J. D. (2001) Intermediate Q from soluble methane monooxygenase hydroxylates the mechanistic substrate probe norcarane: Evidence for a stepwise reaction. *J. Am. Chem. Soc. 123*, 11831–11837.
14. Andersson, K. K., Froland, W. A., Lee, S. K., and Lipscomb, J. D. (1991) Dioxygen independent oxygenation of hydrocarbons by methane monooxygenase hydroxylase component. *New J. Chem. 15*, 411–415.
15. Froland, W. A., Andersson, K. K., Lee, S. K., Liu, Y., and Lipscomb, J. D. (1992) Methane monooxygenase component B and reductase alter the regioselectivity of the hydroxylase component-catalyzed reactions. A novel role for protein-protein interactions in an oxygenase mechanism. *J. Biol. Chem. 267*, 17588–17597.
16. Murray, L. J., Naik, S. G., Ortillo, D. O., Garcia-Serres, R., Lee, J. K., Huynh, B. H., and Lippard, S. J. (2007) Characterization of the arene-oxidizing intermediate in ToMOH as a diiron(III) species. *J. Am. Chem. Soc. 129*, 14500–14510.
17. Moenne-Loccoz, P., Baldwin, J., Ley, B. A., Loehr, T. M., and Bollinger, J. M. Jr. (1998) O_2 activation by non-heme diiron proteins: Identification of a symmetric mu-1,2-peroxide in a mutant of ribonucleotide reductase. *Biochemistry 37*, 14659–14663.
18. Broadwater, J. A., Achim, C., Munck, E., and Fox, B. G. (1999) Mössbauer studies of the formation and reactivity of a quasi-stable peroxo intermediate of stearoyl-acyl carrier protein delta 9-desaturase. *Biochemistry 38*, 12197–12204.
19. Pereira, A. S., Small, W., Krebs, C., Tavares, P., Edmondson, D. E., Theil, E. C., and Huynh, B. H. (1998) Direct spectroscopic and kinetic evidence for the involvement of a peroxodiferric intermediate during the ferroxidase reaction in fast ferritin mineralization. *Biochemistry 37*, 9871–9876.
20. Vu, V. V., Emerson, J. P., Martinho, M., Kim, Y. S., Münck, E., Park, M. H., and Que, L. (2009) Human deoxyhypusine hydroxylase, an enzyme involved in regulating cell growth, activates O_2 with a non-heme diiron center. *Proc. Natl. Acad. Sci. U.S.A. 106*, 14814–14819.
21. Stenkamp, R. E. (1994) Dioxygen and hemerythrin. *Chem. Rev. 94*, 715–726.
22. Pikus, J. D., Studts, J. M., McClay, K., Steffan, R. J., and Fox, B. G. (1997) Changes in the regiospecificity of aromatic hydroxylation produced by active site engineering in the diiron enzyme toluene 4-monooxygenase. *Biochemistry 36*, 9283–9289.
23. Moe, L. A., Hu, Z., Deng, D., Austin, R. N., Groves, J. T., and Fox, B. G. (2004) Remarkable aliphatic hydroxylation by the diiron enzyme toluene 4-monooxygenase in reactions with radical or cation diagnostic probes norcarane, 1,1-dimethylcyclopropane, and 1,1-diethylcyclopropane. *Biochemistry 43*, 15688–15701.
24. Mitchell, K. H., Rogge, C. E., Gierahn, T., and Fox, B. G. (2003) Insight into the mechanism of aromatic hydroxylation by toluene 4-monooxygenase by use of specifically deuterated toluene and p-xylene. *Proc. Natl. Acad. Sci. U.S.A. 100*, 3784–3789.
25. Newman, L. M., and Wackett, L. P. (1995) Purification and characterization of toluene 2-monooxygenase from *Burkholderia cepacia* G4. *Biochemistry 34*, 14066–14076.
26. Pikus, J. D., Mitchell, K. H., Studts, J. M., McClay, K., Steffan, R. J., and Fox, B. G. (2000) Threonine 201 in the diiron enzyme toluene 4-monooxygenase is not required for catalysis. *Biochemistry 39*, 791–799.
27. Otwinowski, Z., and Minor, W. (1997) The processing of X-ray diffraction data collected in oscillation mode. *Methods Enzymol. 276*, 307–326.
28. Vagin, A., and Teplyakov, A. (1997) MOLREP: An automated program for molecular replacement. *J. Appl. Crystallogr. 30*, 1022–1025.
29. Adams, P. D., Grosse-Kunstleve, R. W., Hung, L. W., Ioerger, T. R., McCoy, A. J., Moriarty, N. W., Read, R. J., Sacchettini, J. C., Sauter, N. K., and Terwilliger, T. C. (2002) PHENIX: Building new software for automated crystallographic structure determination. *Acta Crystallogr. D58*, 1948–1954.
30. Emsley, P., and Cowtan, K. (2004) Coot: Model-building tools for molecular graphics. *Acta Crystallogr. D60*, 2126–2132.
31. Murshudov, G. N., Vagin, A. A., and Dodson, E. J. (1997) Refinement of macromolecular structures by the maximum-likelihood method. *Acta Crystallogr. D53*, 240–255.
32. Lovell, S. C., Davis, I. W., Arendall, W. B.III, de Bakker, P. I. W., Word, J. M., Prisant, M. G., Richardson, J. S., and Richardson, D. C. (2003) Structure validation by C-α geometry: ϕ, ψ and C-β deviation. *Proteins: Struct., Funct., Genet. 50*, 437–450.
33. DeLano, W. L. (2002) The PyMOL Molecular Graphics System, DeLano Scientific, San Carlos, CA.
34. Taylor, R. (1990) Electrophilic Aromatic Substitution, p 513, John Wiley & Sons, New York.
35. Rosenzweig, A. C., Frederick, C. A., Lippard, S. J., and Nordlund, P. (1993) Crystal structure of a bacterial non-haem iron hydroxylase that catalyses the biological oxidation of methane. *Nature 366*, 537–543.
36. Sazinsky, M. H., and Lippard, S. J. (2005) Product bound structures of the soluble methane monooxygenase hydroxylase from *Methylococcus capsulatus* (Bath): Protein motion in the α-subunit. *J. Am. Chem. Soc. 127*, 5814–5825.
37. McCormick, M. S., Sazinsky, M. H., Condon, K. L., and Lippard, S. J. (2006) X-ray crystal structures of manganese(II)-reconstituted and native toluene/o-xylene monooxygenase hydroxylase reveal rotamer shifts in conserved residues and an enhanced view of the protein interior. *J. Am. Chem. Soc. 128*, 15108–15110.
38. Lee, S. K., and Lipscomb, J. D. (1999) Oxygen activation catalyzed by methane monooxygenase hydroxylase component: Proton delivery during the O-O bond cleavage steps. *Biochemistry 38*, 4423–4432.
39. Skulan, A. J., Brunold, T. C., Baldwin, J., Saleh, L., Bollinger, J. M. Jr., and Solomon, E. I. (2004) Nature of the peroxo intermediate of the W48F/D84E ribonucleotide reductase variant: Implications for O_2 activation by binuclear non-heme iron enzymes. *J. Am. Chem. Soc. 126*, 8842–8855.
40. Dunietz, B. D., Beachy, M. D., Cao, Y., Whittington, D. A., Lippard, S. J., and Friesner, R. A. (2000) Large scale ab initio quantum chemical calculation of the intermediates in the soluble methane monooxygenase catalytic cycle. *J. Am. Chem. Soc. 122*, 2828–2839.
41. Elsen, N. L., Bailey, L. J., Hauser, A. D., and Fox, B. G. (2009) Role for threonine 201 in the catalytic cycle of the soluble diiron hydroxylase toluene 4-monooxygenase. *Biochemistry 48*, 3838–3846.
42. Kim, K., and Lippard, S. J. (1996) Structure and Mössbauer spectrum of a (μ-1,2-peroxo)bis(μ-carboxylato)diiron(III) model for the peroxo intermediate in the methane monooxygenase hydroxylase reaction cycle. *J. Am. Chem. Soc. 118*, 4914–4915.
43. Hajdu, J., Neutze, R., Sjogren, T., Edman, K., Szoke, A., Wilmouth, R. C., and Wilmot, C. M. (2000) Analyzing protein functions in four dimensions. *Nat. Struct. Biol. 7*, 1006–1012.

44. Saleh, L., Krebs, C., Ley, B. A., Naik, S., Huynh, B. H., and Bollinger, J. M. Jr. (2004) Use of a chemical trigger for electron transfer to characterize a precursor to cluster X in assembly of the iron-radical cofactor of *Escherichia coli* ribonucleotide reductase. *Biochemistry 43*, 5953–5964.
45. Holmes, M. A., Le Trong, I., Turley, S., Sieker, L. C., and Stenkamp, R. E. (1991) Structures of deoxy and oxy hemerythrin at 2.0 Å resolution. *J. Mol. Biol. 218*, 583–593.
46. Karlsson, A., Parales, J. V., Parales, R. E., Gibson, D. T., Eklund, H., and Ramaswamy, S. (2003) Crystal structure of naphthalene dioxygenase: Side-on binding of dioxygen to iron. *Science 299*, 1039–1042.
47. Kovaleva, E. G., and Lipscomb, J. D. (2007) Crystal structures of Fe^{2+} dioxygenase superoxo, alkylperoxo, and bound product intermediates. *Science 316*, 453–457.
48. Simmons, C. R., Krishnamoorthy, K., Granett, S. L., Schuller, D. J., Dominy, J. E. Jr., Begley, T. P., Stipanuk, M. H., and Karplus, P. A. (2008) A putative Fe^{2+}-bound persulfenate intermediate in cysteine dioxygenase. *Biochemistry 47*, 11390–11392.
49. Dong, Y., Yan, S., Young, V. G., and Que, L.Jr. (1996) Crystal structure analysis of a synthetic non-heme diiron-O_2 adduct: Insight into the mechanism of oxygen activation. *Angew. Chem., Int. Ed. 35*, 618–620.
50. Ookubo, T., Sugimoto, H., Nagayama, T., Masuda, H., Sato, T., Tanaka, K., Maeda, Y., Okawa, H., Hayashi, Y., Uehara, A., and Suzuki, M. (1996) *cis*-μ-1,2-Peroxo diiron complex: Structure and reversible oxygenation. *J. Am. Chem. Soc. 118*, 701–702.